The International Journal of Advanced Manufacturing Technology (2022) 121:2243–2255
https://doi.org/10.1007/s00170-022-09473-w

ORIGINAL ARTICLE

Experimental study on ultrasonic vibration-assisted grinding of hardened steel using white corundum wheel

Qiang Huang[1] · Biao Zhao[1] · Yang Cao[1] · Wenfeng Ding[1] · Yucan Fu[1] · Changlan Pu[2] · Menglan Tang[3] · Mingming Deng[3] · Guoliang Liu[3]

Received: 9 February 2022 / Accepted: 31 May 2022 / Published online: 9 June 2022

Abstract

The combination of ultrasonic vibration-assisted grinding (UVAG), the ultrasonic vibrating method, and the conventional grinding (CG) process is proposed to improve the grindability of hardened steel in the CG process. Comparative investigations on grinding force, temperature, and specific grinding energy for both grinding processes were conducted. In addition, the morphologies of the wheel wear and ground surfaces were also studied. Findings show that compared with the CG processes, the normal and tangential grinding forces in UVAG are reduced greatly by 16.44% and 17.44%, respectively. The UVAG process decreases the specific grinding energy by 8.30% owing to the increase of the maximum undeformed chip thickness and the grinding temperature by 19.01% due to the improvement of the coolant heat transfer capacity in the grinding arc zone. Meanwhile, the promising grain sharpness of wheels can be guaranteed from the enhanced cooling function on the grinding arc zone and the grain's micro-fracture caused by ultrasonic impacting actions.

Keywords Grinding temperature · Grinding specific energy · Coolant heat transfer coefficient · Ultrasonic vibration-assisted grinding · Hardened steel

1 Introduction

Hardened steel has been widely used in the automotive and aerospace industries, including automotive crankshafts, cutting tools, bearings, and molds, owing to its superior mechanical properties and high wear-resistances [1, 2]. The existence of high-carbon martensite inside the heat treatment layers of hardened steels is attributed to the overall poor machinability and low thermal conductivity of hardened steel [3, 4]. Grinding processes are employed to eliminate deformation after heat treatment and improve the accuracy of workpieces. However, unexpected grinding burn easily occurs due to the aggregation of high grinding force and heat on the workpiece surface, resulting in poor surface quality and high surface residual tensile stress [5–7]. Thus, a new machining technology is urgently needed to reduce the grinding force and heat, such as the use of ultrasound-assisted grinding with ultrasonic vibrations on a workpiece or grinding wheel [8], high-shear and low-pressure grinding with a new grinding wheel includes the shear thickening abrasive layer [9, 10], and laser-assisted grinding by applying a laser-softened layer to the surface of a workpiece [11].

The ultrasonic vibration-assisted grinding (UVAG) technique, which is an excellent method, has received increasing attention locally and overseas for its ability to significantly improve the grindability of difficult-to-cut materials [12]. Cao et al. [13] performed a comparative study using CG and UVAG processes on nickel-based superalloy and revealed that the tangential and normal grinding forces decreased by 30% and 40%, respectively, due to the acoustic softening and ultrasonic friction reduction effects. Dai et al. [14] reported that the peening effect of abrasive ultrasonic vibration would cause brittle fracture and soften the workpiece surface during the grinding of SiC ceramic materials, resulting in the significant reduction of the normal, tangential, and radial forces by 69%, 52%, and 71%, respectively. Zhang et al. [15]

✉ Biao Zhao
zhaobiao@nuaa.edu.cn

[1] National Key Laboratory of Science and Technology On Helicopter Transmission, Nanjing University of Aeronautics and Astronautics, Nanjing 210016, China

[2] Avic Cheng'du Aircraft Industrial (Group) Co, LTD, Chengdu 610092, China

[3] AECC Zhongchuan Transmission Machinery Co., LTD, Changsha 410200, China

reported that the average undeformed chip thickness could be reduced during the machining or removal of brittle C_f/SiC composites via UVAG processes because the interference of the abrasive trajectory results in intermittent non-cutting processes. Here, the normal and tangential forces were decreased by 20.44% and 17.66, respectively. Along this line of consideration, the employment of ultrasonic vibrating methods in traditional machining processes can reduce the grinding forces and temperature and thus improve the machining surface integrity and the tools' wear-resistance ability. However, the removal characteristics and grinding heat transfer mechanism of hardened steel materials have yet to be fully investigated under UVAG processes.

Furthermore, sudden grinding burn usually occurs due to the accumulation of grinding heat on the machining surface, which has a devastating influence on the blockage of grinding wheels and is associated with ground surface quality [16, 17]. In recent decades, numerous researchers have focused on controlling the generation [18] and conduction [19] of grinding heat. Malkin and Guo [20] reported that the grinding temperature could be availably reduced by controlling the grinding specific energy. Here, the reduction in grinding specific energy ranged from 105 to 70 J/mm^3, resulting in a 33% reduction in grinding temperature. Single et al. [21] performed theoretical modeling and experimental research on the different components of specific grinding energy, including the energy of chip formation and primary and secondary rubbing and ploughing, contributing to the prediction of the specific grinding energy. Subsequently, Jeager and Carslaw [22] proposed a one-dimensional moving heat source model to connect the heat flow into the workpiece with the internal temperature field, providing a theoretical basis for grinding thermal analysis. On the basis of the model established by Jaeger and Carslaw [22], Rowe [23] analyzed the four conduction modes of the total grinding heat and the theoretical model of heat distribution, clarifying the influence of the material's physical parameters and the grinding parameters on the grinding temperature. Lavisse et al. [24] conducted high-flow and high-speed jet grinding experiments, which greatly reduced the grinding heat absorbed by workpieces, resulting in a 50% reduction in heat distribution ratio and maximum temperature in the grinding arc zone. Therefore, grinding thermal analysis must be further performed to control the grinding temperature during CG and UVAG processes.

In this study, comparative experiments were conducted to study the effect of ultrasonic vibration and grinding parameters on the grindability of hardened steel under CG and UVAG processes. Following the introduction part, the experimental setup and the associated equipment are presented in the Sect. 2. Subsequently, the Sect. 3 reveals the influence of ultrasonic vibration processes and grinding parameters on the grinding force, the grinding specific energy, the coolant heat transfer coefficient, the grinding surface temperature, wheel wear, and the grinding surface defects. Finally, the Sect. 4 is summarized in the last section.

2 Experiment environment

2.1 Experimental setup

In this trial, grinding operations were performed using a surface grinder (Blohm Profimat MT-408), and white corundum grinding wheels (WA80F13V45m) were used. The corresponding experiment setup and the grinding device are shown in Fig. 1. The left part of Fig. 1 shows that an ultrasonic vibration platform system was used, and the ultrasonic generator generates a high-frequency vibration signal [13]. Subsequently, tangential vibration is generated in the center area of the platform by amplifying the amplitude of the horn. In this study, GCr15 hardened steel was adopted as the workpiece material with dimensions of 30 mm × 10 mm × 12 mm (L × W × H), and the hardness of the material can reach HRC 60–62 within a depth of 2 mm from the surface. The material composition of GCr15 hardened steel is listed in

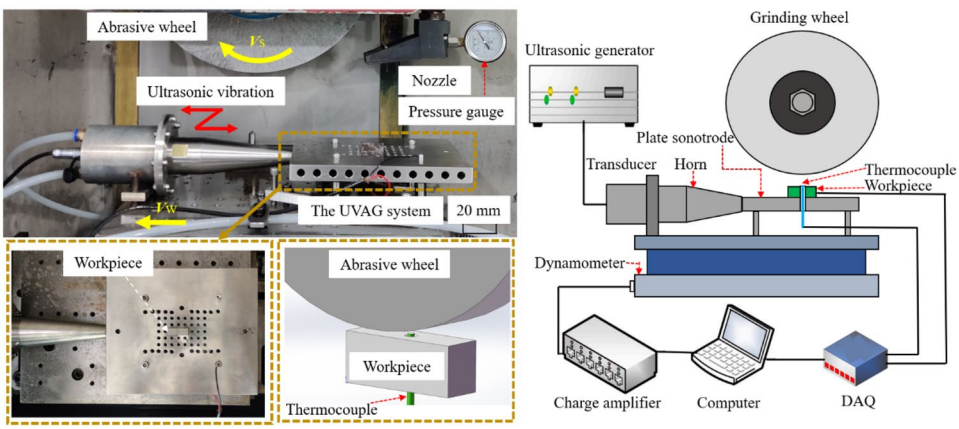

Fig. 1 Schematic of experimental setup and grinding equipment

Table 1 Material components of GCr15 hardened steel (%)

Material	C	Si	Mn	P	S	Cr	Ni	Mo	Fe
GCr15	1.03	0.227	0.353	0.007	0.003	1.46	0.015	0.0096	Balance

Table 1. In addition, Table 2 shows some typical thermal performance values of the workpiece and grinding wheel materials used for the further investigation of the coolant heat transfer coefficient during grinding processes. Furthermore, a sealed shell was adopted to keep the UVAG system running stably under the coolant, and then air cooling was continuously injected to maintain the proper working temperature inside the transducer.

Prior to the grinding operation, the vibration frequency and amplitude of the workpiece without loads were calibrated. Here, three uniform points on the end face of the workpiece were selected, and a laser doppler vibrometer was used to measure the amplitude and the sample frequency, which were fixed at 480 kHz. The real-time FFT analysis using the Quick SA software revealed that the workpiece can produce a stable ultrasonic amplitude (A) of 4 μm when the ultrasonic generator power is 19% and the vibration frequency f is 19.70 kHz. Subsequently, the UVAG system was fixed on the grinder platform through the platen. During the experiment, surface grinding was carried out 5 times using the parameters in Table 3, and the grinding force and temperature were recorded. A water-based coolant containing 5% emulsion was used. After the experiment, to eliminate the influence of the wear of the grinding wheel and the difference in surface quality after multiple grinding, uniform grinding parameters were used to dress the surface of the workpiece (grinding speed of $v_s = 25$ m/s, workpiece speed of $v_w = 7.5$ m/min, depth of cut of $a_p = 15$ μm). Then, a dressing diamond was used to trim the grinding wheel to maintain the ability to cut materials, and the trimming parameters are $v_{st} = 20$ m/s, $v_{wt} = 200$ mm/s, and $a_{pt} = 100$ μm.

2.2 Testing method

During this comparative experiment, a four-phase piezoelectric dynamometer (Kistler 9253B) and a multi-channel charge amplifier (Kistler 5080A) were employed to measure the grinding forces. In addition, as shown in Fig. 2, a semi-artificial thermocouple was applied to obtain the thermoelectric signals recorded by the NI USB-6211 DAQ card and processed by the NI-LabView software. Then, the grinding temperature could be calculated using the relationship between the actual temperature (T) and thermoelectric value (E). Here, this relationship was achieved via the standard calibration method and is expressed as follows [25]:

$$T = -0.0223E^2 + 18.2532E - 6.0770 \quad (1)$$

After the grinding processes, the machined workpiece should be ultrasonically cleaned with 75% alcohol. After the grinding experiments, the abrasive layer of the grinding wheels for both CG and UVAG processes was broken into small pieces, which were cleaned through the same cleaning methods to reveal the influence of grinding processes on wheel wear. Subsequently, these pieces of wheels were detected by scanning electron microscopy (Quanta 200).

Table 2 Thermal properties of aluminum oxide and GCr15 hardened steel

Material	Conductivity k (W/mK)	Density ρ (kg/m^3)	Specific heat c (J/kgK)	Thermal property $\beta = \sqrt{k\rho c}$ (J/m^{2}sK)
GCr15	34.3	7815	506	11,650
Aluminum oxide	35.0	3980	765	10,300

3 Results and discussion

3.1 Grinding forces

Grinding forces, as an important indicator, have a great influence on the grinding specific energy, the grinding temperature, the grinding wheel performance, and the ground surface quality [26]. Figure 3 shows the influence of grinding parameters on normal force F_n and tangential force F_t during the CG and UVAG processes. When the grinding speed (v_s) rises from 15 to 30 m/s, the normal and tangential forces of CG decrease from 103.95 to 63.91 N and 46.17 to 29.45 N, respectively, as illustrated in Fig. 3a. A similar varying tendency with F_n and F_t can be observed in the UVAG

Table 3 Grinding process parameters for both grinding processes

Contents	Values
Machine tool	Surface Grinder Blohm Profimat MT-408
Grinding mode	Surface down grinding
Abrasive wheel	White alundum wheel (WA/80F13V45m)
Grinding speed v_s	15–30 m/s
Workpiece speed v_w	4.5–9 m/min
Depth of cut a_p	10–25 μm
Grinding width b	10 mm
Cooling condition	5% emulsified water; pressure at 0.2 MPa

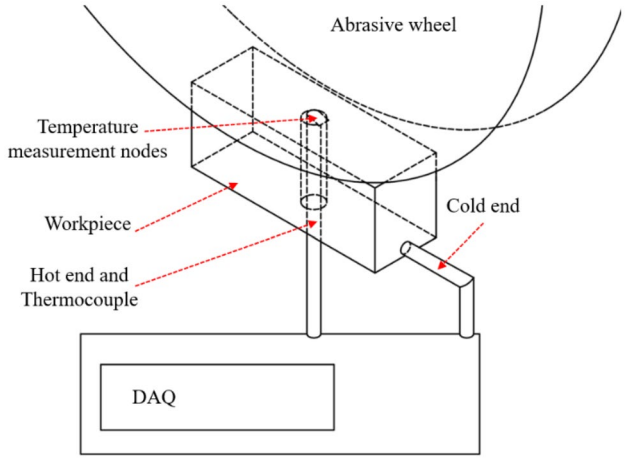

Fig. 2 Schematic of semi-manual thermocouple temperature measurement

process compared to the other one, while the normal and tangential forces are lower than those in the other process by 5.07 N (6.98%) and 2.33 N (7.91%), respectively. However, the difference is small with the change in grinding speed, indicating that grinding speed has a little significant effect on the ability of UVAG in terms of reducing the grinding forces. In addition, the F_n and F_t of CG/UVAG increase with workpiece speed v_w (Fig. 3b). Meanwhile, the maximum difference between the normal and tangential forces in UVAG and CG occurs at the maximum feed speed (v_w) of 9 m/min, namely, 7.27 N (8.94%) and 4.45 N (12.19%), respectively. The abrasive particles are in contact and separated in a single vibration cycle in UVAG, like a tool in a constant cutting-separating state. The separation condition of the grinding wheel and the workpiece can be expressed as follows [27]: $v_w < 2\pi fA$. The intermittent grinding phenomenon between the abrasive particles and the workpiece is likely to occur due to the increase in the workpiece feed speed. As illustrated in Fig. 3c, the F_n and F_t of CG and UVAG increase with the depth of cut a_p. However, the differences between the F_n and F_t in UVAG and CG are most obvious at a small cutting depth ($a_p = 10$ µm) and decrease by 9.46 N (16.44%) and 4.8 N (17.44%), respectively, indicating that the UVAG process with a soft WA wheel is suitable for the

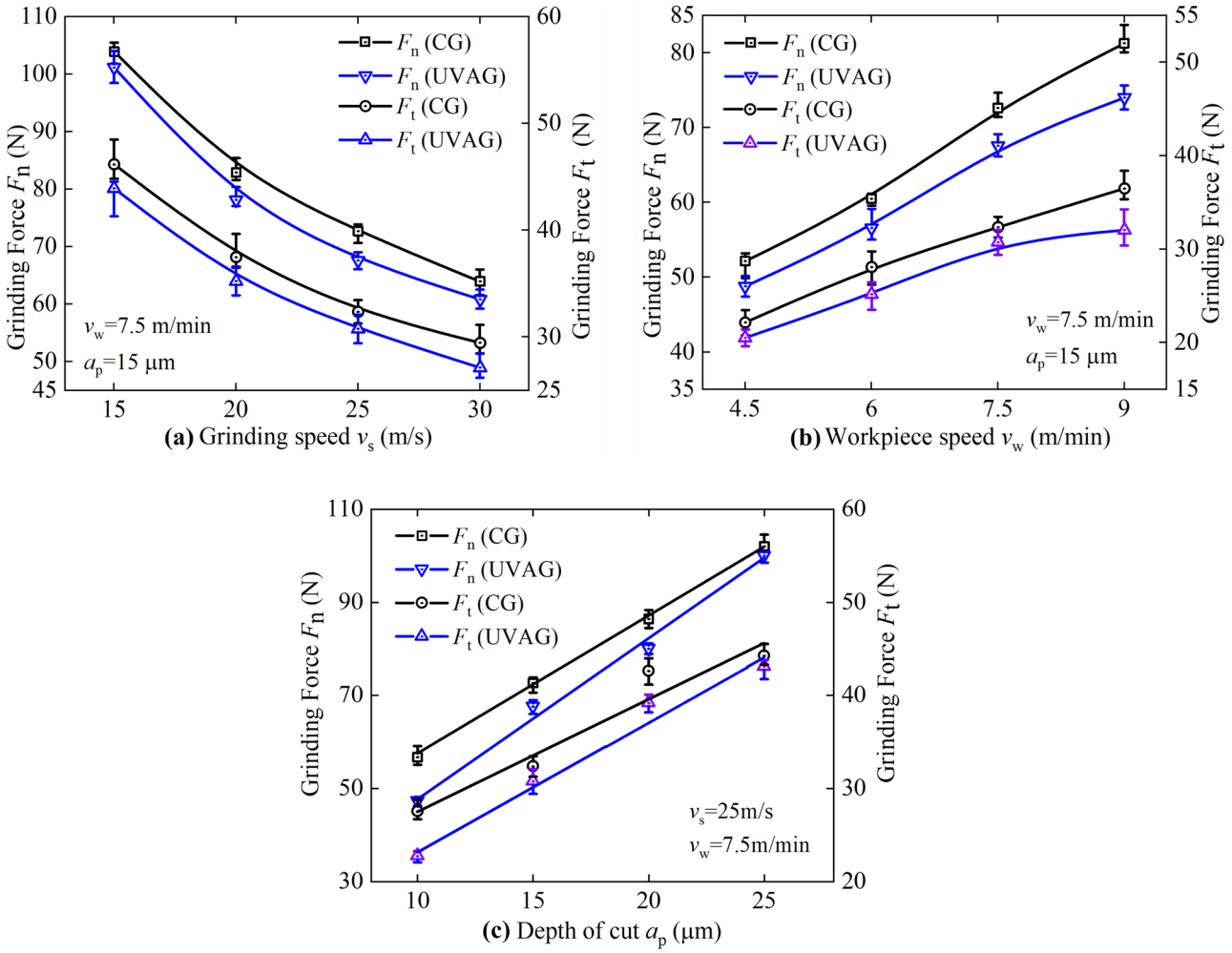

Fig. 3 Effects of grinding parameters on grinding forces during CG and UVAG processes

small cutting depth. For a large cutting depth, little difference exists between the grinding forces in the UVAG and CG processes. This phenomenon mainly occurs because although ultrasonic vibration improves the self-sharpening effect of grains [28], it will accelerate the wheel wear under a large depth of cut, presenting a similar grinding force in UVAG and CG at the large depth of cut.

3.2 Specific grinding energy

Specific grinding energy e_s, which is an important indicator for evaluating the degree of difficulty in removing materials and measuring the generated heat during grinding processes, presents the consumed energy by removal materials per volume, which can be expressed as follows:

$$e_s = \frac{P}{v_w a_p b} = \frac{F_t v_s}{v_w a_p b} \tag{2}$$

where the grinding width (b) of the workpiece is fixed at 10 mm.

To investigate the specific grinding energy clearly, the maximum undeformed chip thickness should be studied [29]. Here, as mentioned by Pahlitzsch and Helmerdig [30], maximum undeformed chip thickness a_{gmax} can be obtained using the following expression (Eq. (3)), considering the adjacent abrasive grains with the same spacing of grinding wheels.

$$a_{g\max} = 2\frac{\lambda_s v_w}{v_s}\sqrt{\frac{a_p}{d_s}} \tag{3}$$

where λ_s is the grinding edge spacing, and d_s is the grinding wheel diameter.

In Fig. 4, the evolution of the specific grinding energy (e_s) affected by the grinding wheel speed, the feed speed, and the depth of cut is plotted. As grinding speed v_s increases from 15 to 30 m/s under at feed speed v_w of 7.5 m/min and cutting depth a_p of 15 μm, the specific grinding energy (e_s) of CG increases from 36.94 to 47.12 J/mm^3 by 27.56%, and that of UVAG increases from 35.14 to 43.39 J/mm^3 by 23.48% (Fig. 4a). Figure 4b shows that as the v_w value increases from 4.5 to 9 m/min at the v_s of 25 m/s and a_p of 15 μm, the e_s value of CG decreases from 49.22 to 40.56 J/mm^3 by 17.59%, and that of UVAG decreases 45.58 to 35.61 J/mm^3 by 21.87%. As a_p increases from 10 to 25 μm, the e_s value of CG decreases by 35.68% from 55.04 to 35.40 J/mm^3, and that of UVAG decreases by 24.14% from 45.44 to 34.47 J/mm^3 (Fig. 4c). Figure 4d demonstrates that e_s decreases with the rise of a_{gmax} according to Eq. (3). The e_s of UVAG is reduced in the range of 5.30–11.29% compared with that of CG. Meanwhile, the decreasing tendency of e_s with the increase of a_{gmax} reveals that UVAG has better grindability and lower grinding energy consumption and grinding heat generation than CG. This phenomenon can be explained in view of the different material removal stages (e.g., scratching, ploughing, and cutting) of abrasive grains. Great energy is consumed in scratching and ploughing due to the size effect according to Eq. (3). Here, a_{gmax} is increased with the decrease of v_s and rise of v_w and a_p, which is reflected in the reduction of e_s.

To clearly investigate the influence of ultrasonic vibration parameters on material cutting processes, the a_{gmax} model of the UVAG methods was established based on traditional grinding processes, as illustrated in Fig. 5. Here, the a_{gmax} value (Eq. (4)) could be rewritten using the line EH and clamping angle θ.

$$a_{gmax} = EH = EF \cdot \sin\theta \tag{4}$$

According to the coordinate system in Fig. 4, the moving trajectory of two continuous abrasive grains with a distance of λ_s during the UVAG processes could be expressed as follows:

$$\begin{cases} x_{u,i} = v_w t + A\sin(\omega t) + R\sin(\frac{v_s}{R}t) \\ y_{u,i} = R - R\cos(\frac{v_s}{R}t) \\ x_{u,i-1} = v_w(t + \frac{\lambda_s}{v_s}) + A\sin(\omega(t + \frac{\lambda_s}{v_s})) + R\sin(\frac{v_s}{R}t) \\ y_{u,i-1} = R - R\cos(\frac{v_s}{R}t) \end{cases} \tag{5}$$

where A is the ultrasonic amplitude, ω is the ultrasonic angular velocity, t is the current time, and R is the radius of the grinding wheel. From Eq. (5), the following equation could be presented:

$$EF_u = x_{u,i-1} - x_{u,i} = \frac{\lambda_s v_w}{v_s} + A\sin(\omega(t + \frac{\lambda_s}{v_s})) - A\sin(\omega t) \tag{6}$$

In this case, a_{gmax} must be calculated within a period, that is, $t = -\lambda_s/(2v_s)$. Here, the maximum value of EF_u should be

$$EF_{u,\max} = \frac{\lambda_s v_w}{v_s} + 2A\sin(\omega\frac{\lambda_s}{2v_s}) \tag{7}$$

After simplification,

$$\sin\theta = \frac{\sqrt{d_s^2 - (d_s - 2a_p)^2}}{d_s} = \frac{\sqrt{4d_s a_p - 4a_p^2}}{d_s} \text{ becomes } \sin\theta = 2\sqrt{\frac{a_p}{d_s}} \tag{8}$$

Therefore, the maximum undeformed chip thickness ($a_{u,gmax}$) of UVAG could be concluded as

$$a_{u,g\max} = 2(\frac{\lambda_s v_w}{v_s} + 2A\sin(\frac{\omega\lambda_s}{2v_s}))\sqrt{\frac{a_p}{d_s}} \tag{9}$$

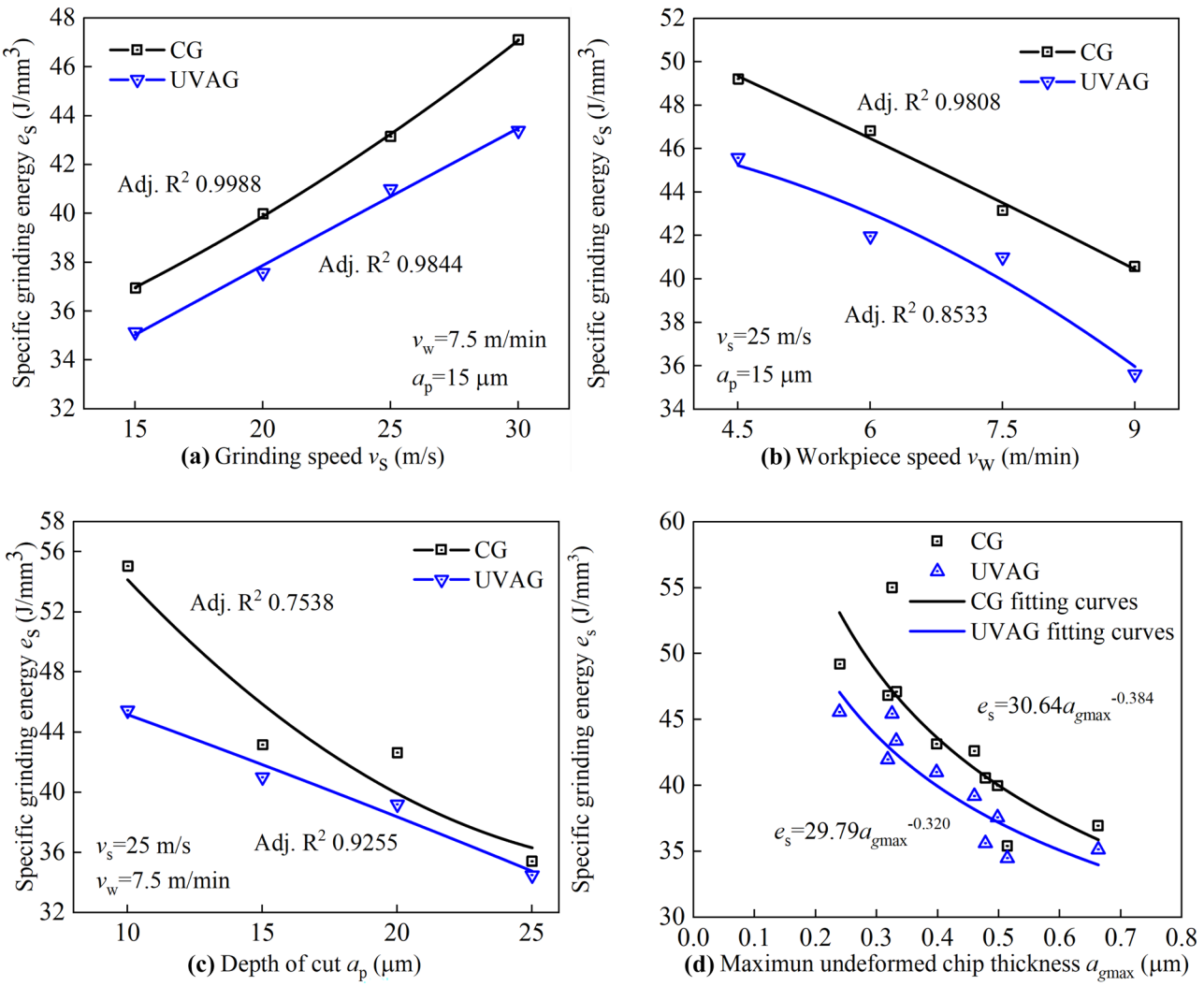

Fig. 4 Effects of grinding parameters and maximum undeformed chip thickness on the specific grinding energy

According to this line of consideration based on Eq. (9), the maximum undeformed chip thickness ($a_{u,gmax}$) was remarkably affected by the ultrasonic vibrating and grinding parameters. Moreover, the phenomenon of intermittent cutting processes between the abrasive grain and the workpiece could be expressed by the $a_{u,gmax}$ model

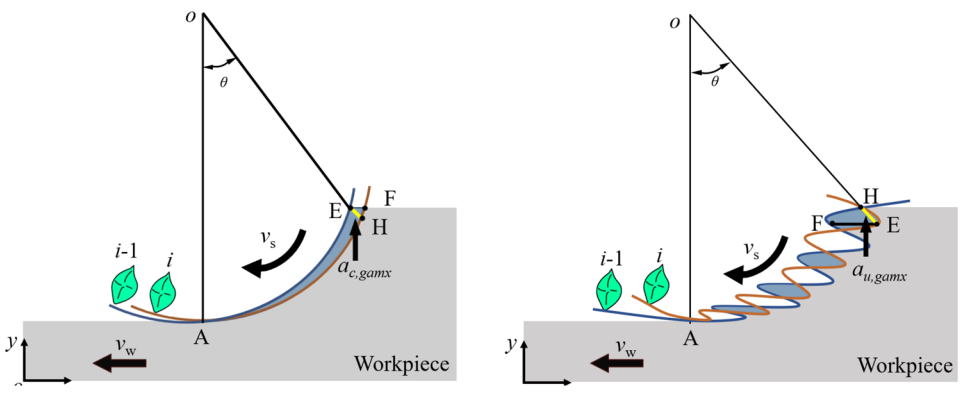

Fig. 5 Schematic of chip formation and maximum undeformed cutting thickness for both grinding methods

(see Eq. (9)) and illustrated by the diagram (see Fig. 5). Figure 6 shows the relationship between $a_{u,gmax}$ and the ultrasonic amplitude and the specific grinding energy. The actual value of the $a_{u,gmax}$ of UVAG is larger than that of CG, and the entering speed of the former's cutting stage is faster than that of the latter. Under the grinding parameters (e.g., grinding speed of 25 m/s, feed speed of 7.5 m/min, and cutting depth of 15 μm) and the ultrasonic amplitude of 4 μm, the $a_{u,gmax}$ of UVAG increased by 25.4% compared with that of CG according to Eq. (9). When amplitude A is 0, $a_{u,gmax}$ and a_{gmax} are equal. Finally, the fitting curves for $a_{u,gmax}$ versus e_s are plotted in Fig. 6b and show a very close fit between UVAG and CG because the UVAG fitting curve corrects the effect of vibration on the thickness of the cut, ultimately showing the relationship between the removal energy of the material and the chip thickness, regardless of whether ultrasound is applied. This phenomenon also proves that Eq. (9) can predict the chip thickness of the UVAG and explains that the ability of the UVAG to reduce e_s decreases with the increase of $a_{u,gmax}$.

3.3 Grinding temperature and coolant heat transfer coefficient

During the grinding processes, a certain amount of energy is required to remove materials, and most of this energy would be converted into heat. Here, heat is transmitted to the workpiece surface, resulting in grinding burns and eventually affecting the service life of the workpiece [31]. Figure 7 illustrates the relationship between the grinding temperatures and parameters for both grinding methods. As the grinding wheel speed rises from 15 to 30 m/s, the grinding temperature of CG rises from 87.80 to 100.68 ℃, and the grinding temperature of UVAG increases from 77.22 to 90.25 ℃. Here, the grinding temperature of UVAG is generally lower than that of CG, showing a decrease of 10.36 to 12.48%. The grinding temperature rises with feed speed v_w, as shown in Fig. 7b. The tendency of the grinding temperature of UVAG and CG is similar, but the temperature of UVAG decreased by 7.08–12.02 ℃ (10.82–19.01%) compared with that of CG. In addition, the grinding temperature of CG and UVAG increases with the a_p (see Fig. 7c), and the grinding temperature of UVAG is always lower than that of CG, ranging from 7.78 to 13.40 ℃ (5.84–17.45%). This phenomenon reveals that the grinding temperature can be effectively reduced by employing ultrasonic vibrating techniques in the traditional grinding processes because of the small e_s value under the same $a_{u,gmax}$.

During the grinding processes, the total grinding heat flux (q_t) is transmitted into various parts, including the workpiece (q_w), the grinding wheel (q_s), the chip (q_{ch}), and the coolant (q_f) [18]. Here, the total heat flux is deduced as

$$q_t = q_w + q_s + q_{ch} + q_f \tag{10}$$

where

$$q_t = \frac{F_t v_s}{b l_c} \tag{11}$$

As an effective method of avoiding grinding burns, the coolants' heat transfer coefficient (h_f) can be expressed via the following formulas.

First, on the basis of the "fluid wheel" hypothesis, the thermal performance (β_f) of coolants is considered, and the coolant is not boiling [23]. In this case, the heat transfer coefficient can be written as

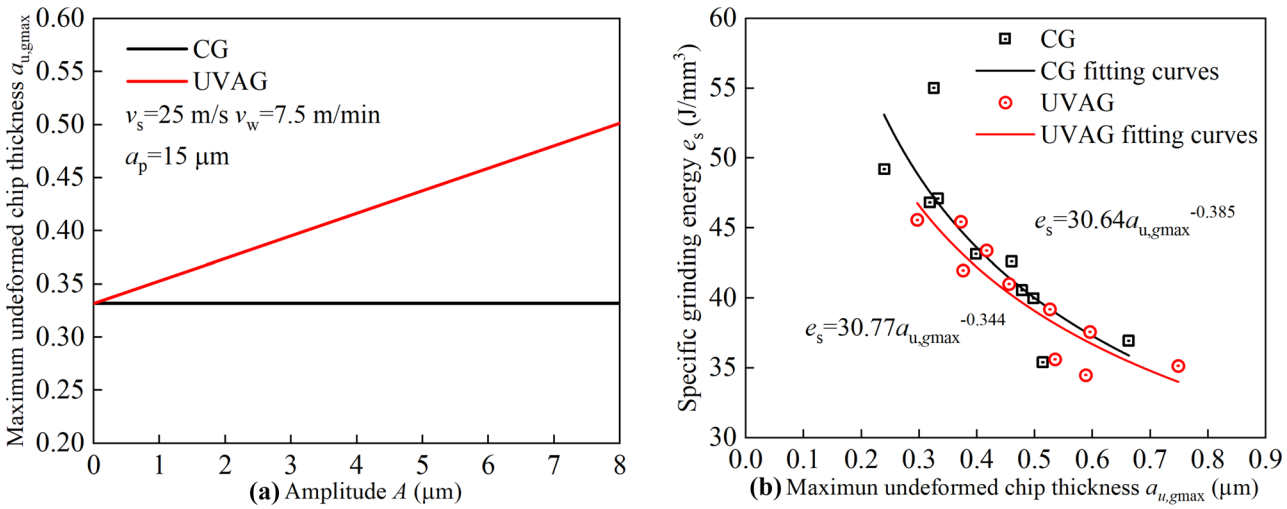

Fig. 6 Plotted curves between the $a_{u,gmax}$ and amplitude and specific grinding energy

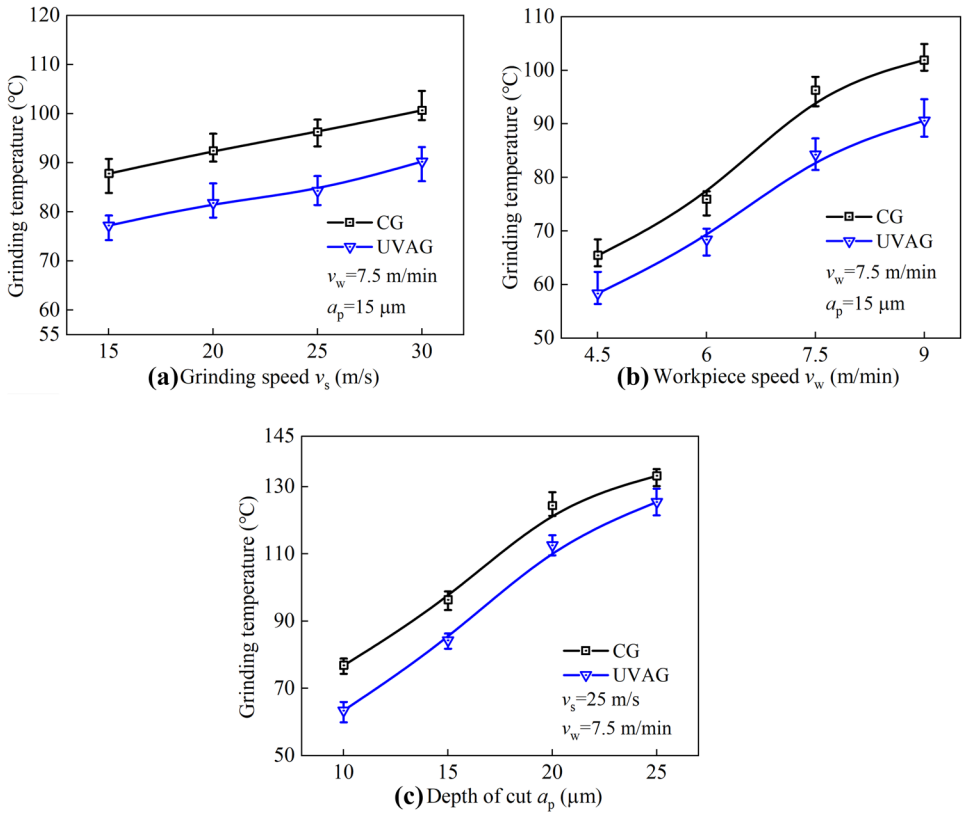

Fig. 7 Grinding temperature versus different grinding parameters

$$h_{f,\mathrm{FW}} = 0.94\,\beta_f \sqrt{\frac{v_s}{l_c}} \tag{12}$$

Then, when the coolant flowing through the grinding arc zone is regarded as a laminar outward sweep plate, the thermal conductivity and specific heat coefficient of the water-based coolant are considered based on the similarity principle of fluid mechanics [32]:

$$h_{f,\mathrm{LW}} = 0.759 \sqrt{\frac{v_s}{l_c}} \tag{13}$$

Finally, the coolants' heat transfer coefficient is confirmed by backtracking the experimental data, which is also the method adopted in this paper. Here, the convective heat transfer coefficient of coolant $h_{f,exp}$ is presented as [33]

$$h_{f,\mathrm{exp}} = \frac{q_t - h_{ch} T_{\mathrm{ch}}}{T_{\max} - T_0} - \frac{h_{\mathrm{w}}}{R_{ws}} = \frac{\frac{F_t v_s}{b l_c} - \rho_w \cdot c_{\mathrm{w}} \cdot T_{\mathrm{ch}} \cdot \frac{a_{\mathrm{p}} v_{\mathrm{w}}}{l_c}}{T_{\max} - T_0} - \frac{\beta_{\mathrm{w}}}{C} \sqrt{\frac{v_{\mathrm{w}}}{l_c}} \cdot \left[1 + \frac{0.97 k_g}{\beta_w \sqrt{r_g v_s}}\right] \tag{14}$$

where l_c is the contact length, ρ_{w} is the workpiece density, c_{w} is the specific heat conductivity, T_{ch} is the chip melting temperature, β_{w} is the thermal performance of the workpiece, k_{g} is the thermal conductivity coefficient of the abrasive particles, C is the temperature factor, and r_g is the effective contact radius of the abrasive particles (20 μm in this article) [23].

Figure 8 shows the effect of grinding speed v_{s} and depth of cut a_{p} on the coolant's heat transfer coefficient according to Eq. (14). The coolant heat transfer coefficient increases with the increase of the wheel speed and the decrease of the cutting depth, which is consistent with the "fluid wheel" (see Eq. (12)) and laminar flow models (see Eq. (13)). The comparison of the bar charts suggests that the coolant's heat transfer coefficient of UVAG is higher than that of CG by 1.87–11.2%. Meanwhile, the strengthening effect of ultrasonic vibration on the heat transfer coefficient weakens as the grinding speed increases. Here, the reduction of the grinding temperature caused by UVAG indicates that ultrasonic vibration improves the convective heat transfer capacity of coolants, reducing the heat flux allocated to the workpiece. Furthermore, the low grinding temperature of UVAG shows that the ultrasonic vibration improves the convective heat transfer capacity of the coolant, leading to a decrease in the heat flux allocated to the workpiece.

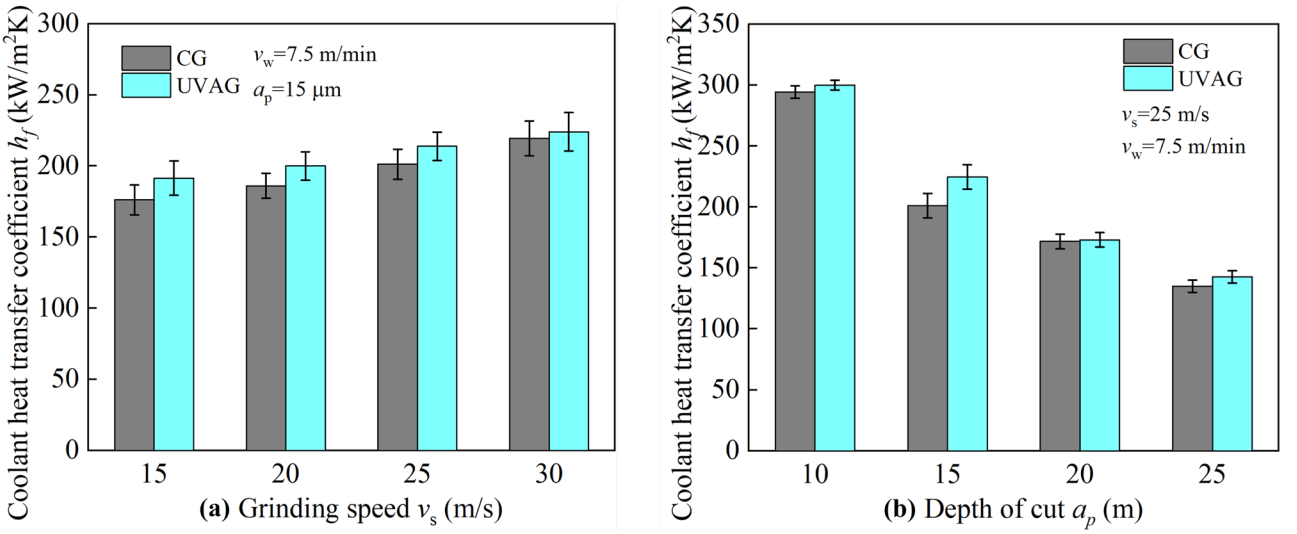

Fig. 8 Coolant heat transfer coefficient versus the grinding speed and depth of cut

During the grinding processes, the coolant in the grinding arc zone is normally regarded as the laminar fluid with the same grinding speed [32, 33], and its convective heat transfer capacity is usually measured with the thickness of the thermal boundary layer. Generally, the heat transfer coefficient with ultrasonic vibrating effects increases by 20–400% compared to traditional processes due to the strengthening effect on the fluid heat transfer of vibrations. Here, the degree depends on the vibration intensity and vibration system [34–36]. Figure 9 illustrates the convection heat transfer mechanism of the coolants under the influence of ultrasonic vibrations. The implosion of cavitation bubbles near the solid–liquid interface will destroy the thermal and velocity boundary layers due to the cavitation or acoustic flow under low–frequency ultrasonic vibration of 20–100 kHz, reducing the thermal resistance and producing micro-turbulence. Meanwhile, the wall of the workpiece vibration will disturb the laminar coolant flow boundary layer near the grinding arc surface and then increase the turbulence intensity. In this case, the fluid thermal boundary layer thickness in the grinding arc zone becomes thinner and the heat transfer capacity of the coolant in the grinding arc zone is thus enhanced. However, the strengthening effect of vibration is not obvious under a high grinding speed due to the thin wall of the thermal boundary layer and great ability of heat transfer, resulting in the large flow Reynolds number and turbulence of the coolant. This phenomenon reveals that the ultrasonic cooling fluid heat transfer ability will decrease as the grinding speed increases. Moreover, Fig. 5 and Eq. (5) show that the "cutting-separating" phenomenon exists during the removal process of abrasive grains. At the separating stage, the gap between the grinding wheel and the workpiece increases;

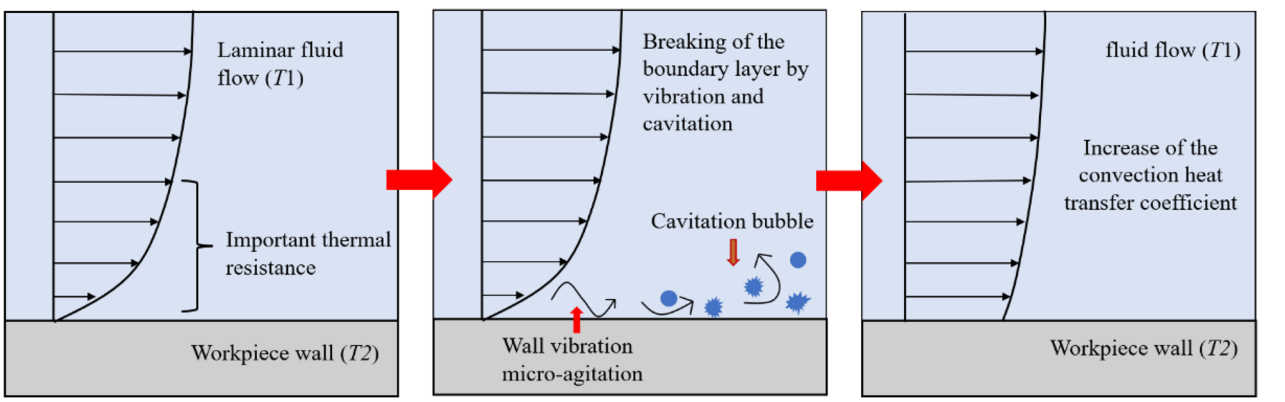

Fig. 9 Diagram of the heat transfer enhancement mechanism by employing ultrasonic vibrations

thus, the coolant flows into the sliding surface between the grain and the workpiece, contributing to the heat dissipation of the contacting interface.

3.4 Wear surface topography

Figure 10 describes the typical SEM morphology and associated schematic images of the wheel wear surface under the CG and UVAG processes to reveal the effect of the ultrasonic vibrating process on the wear behaviors of grinding wheels. Figure 10a, b shows that material adhesion can be clearly observed under the CG processes, and the top surface of the abrasive grains adheres to the cloud-like grinding material. Here, the chip and the adhesive are mixed. As illustrated in Fig. 10c, the long chips generated during the CG processes are more difficult to remove from the wheel–workpiece interface than the shorter chips. In addition, the cutting point temperature of the abrasive particles is much higher than the average grinding temperature during the removal of materials [37]. In this case, the adhesion of chips is easy to observe on the top of abrasive grains under thermal and mechanical actions. When ultrasonic vibration is applied in the grinding processes, no adhesion wear is found on the top of the abrasive grains. However, micro-fracture can be observed, as shown in Fig. 10c, d. As depicted in Fig. 10f, the short chips are easier to produce and escape from the grinding zone due to the "intermittent cutting" of abrasive particles. Meanwhile, the coolant can enter and cool the machined surface during the separation period for UVAG, and the cutting point temperature of the abrasive particles is consequently much lower than that of CG. Moreover, multiple cutting edges are likely to form at the top of the abrasive grains owing to the influence of alternating loads, which can effectively keep the sharpness of the abrasive grain and thus reduce the grinding temperature.

3.5 Ground surface topography

The machined surface roughness (R_a) was measured using a Mahr M2 roughness meter. The results show that the ground roughness (R_a) values for CG and UVAG are 0.223 and 0.201 under the grinding condition of $v_s = 25$ m/s, $v_w = 7.5$ m/min, and $a_p = 25$ μm, respectively. Figure 11 shows the typical ground surface topography detected by 3D confocal microscopy for both grinding processes. The peek-to-peek values for the height of grooves on the ground surface in CG and UVAG are from − 4.021 to 4.109 μm and from − 2.873 to 1.155 μm, respectively. Clearly, the UVAG process exhibits a better surface quality than the other process due to the repeated ironing effect of ultrasound and a smaller associated R_a value.

Figure 12 shows the typical ground surface topography detected by SEM for both grinding processes under the following grinding conditions: $v_s = 25$ m/s, $v_w = 7.5$ m/min,

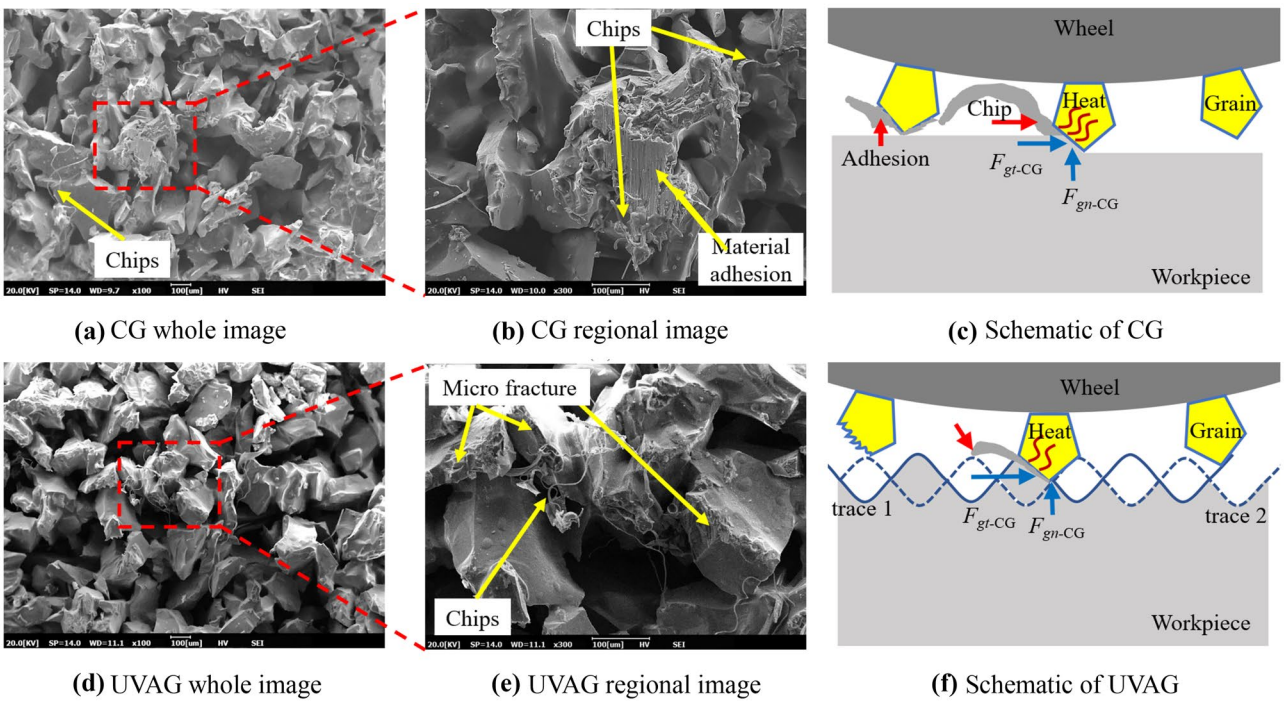

Fig. 10 SEM microstructures and schematic image of wheels surface under CG (**a**, **b**, **c**) and UVAG (**d**, **e**, **f**) processes ($v_s = 25$ m/s, $v_w = 7.5$ m/min, $a_p = 25$ μm)

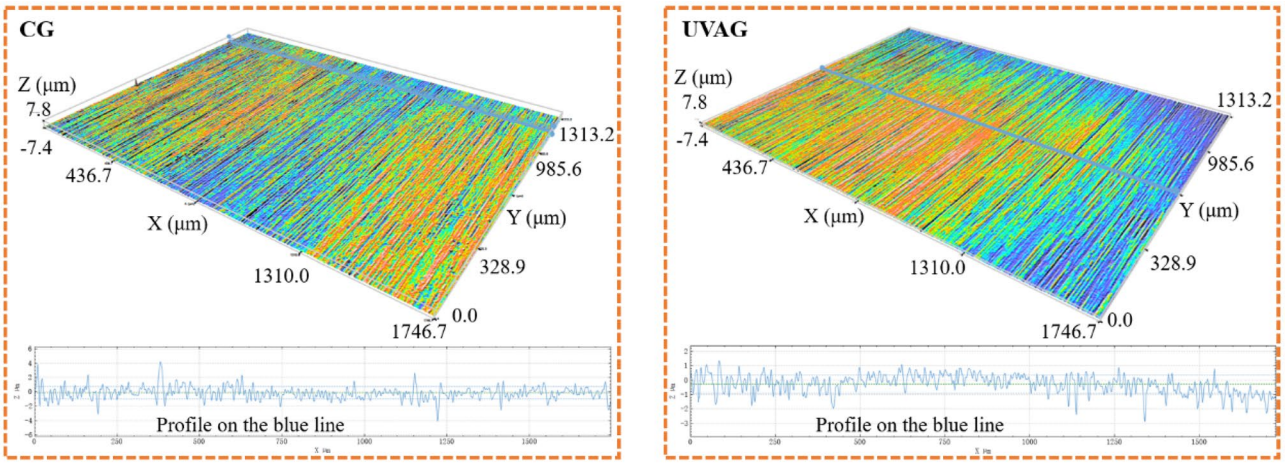

(a) CG **(b)** UVAG

Fig. 11 Ground surface profile produced by CG (**a**) and UVAG (**b**) (v_s = 25 m/s, v_w = 7.5 m/min, a_p = 25 μm)

and a_p = 25 μm. As illustrated in Fig. 12a, b, many surface defects emerge in the CG processes under the influence of mechanical and thermal actions, such as scratches, fracture, smearing, and redeposited materials. However, none of these surface defects can be observed on the surface after UVAG processes in Fig. 12c, d. Moreover, no obvious traces of side flow, ploughing, and striation can be observed on the surfaces of UVAG. Given the squeezing action between abrasive grains and the workpiece, the long chip and large broken grain appear easily, resulting in the formation of grinding scratches, fracture, and redeposited material on the surface of CG. However, the grinding temperature of UVAG is

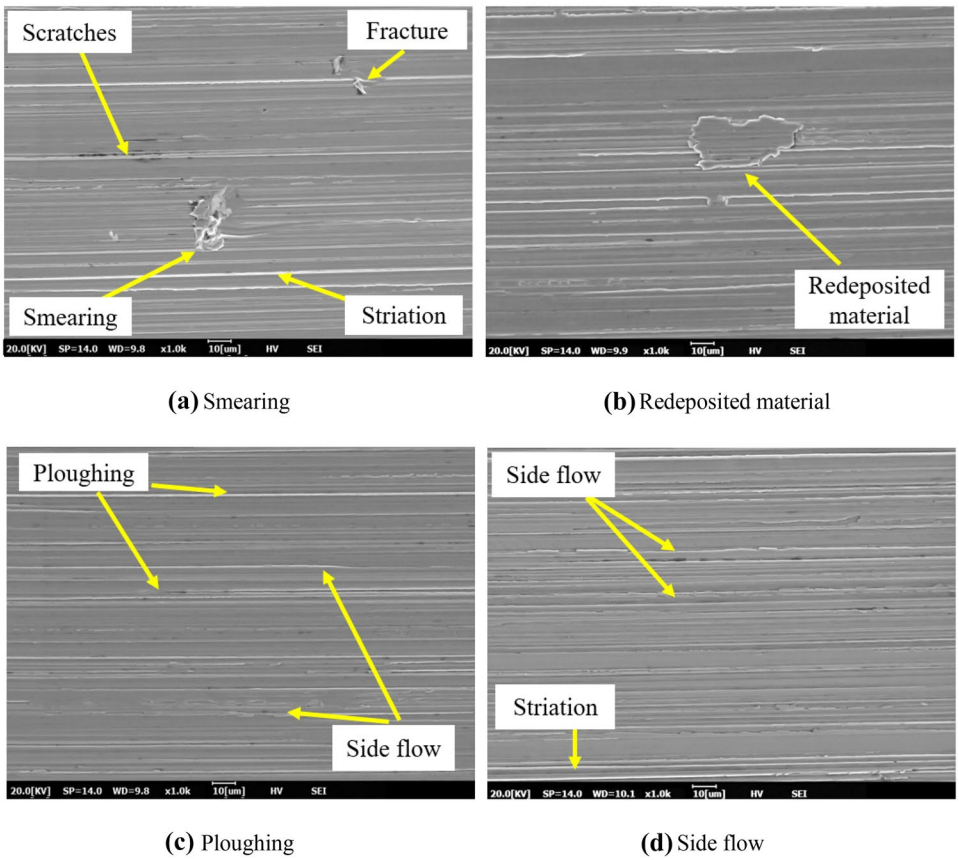

(a) Smearing **(b)** Redeposited material

(c) Ploughing **(d)** Side flow

Fig. 12 Ground surface morphologies after CG (**a**, **b**) and UVAG (**c**, **d**) processes (v_s = 25 m/s, v_w = 7.5 m/min, a_p = 25 μm)

lower than that of CG, the adhesion and diffusion wear are small, and the abrasive particles are prone to the formation of micro-fractures under the ultrasonic impacts of workpieces [28]. Therefore, the grinding sharpness of the abrasive grains in the UVAG processes can be kept stable for a long time, and their ground surface quality is greater than that of the CG processes owing to the few grinding surface defects. In addition, multiple micro ploughing and scratches can be produced due to the axial movement of the workpiece under multi-mode vibration, reducing the accumulation of removed materials and thus improving the grinding quality [38].

4 Conclusions

In this work, comparative trials on the grindability of hardened GCr15 steel were conducted using the white alundum wheels under the CG and UVAG processes. The influences of the grinding and ultrasonic vibrating parameters on the grinding forces, the grinding specific energy, the coolant's convection heat transfer coefficient, the grinding temperature, the wheel wear, and the ground surface quality are discussed exhaustively. The main conclusions are summarized as follows.

1. The UVAG process has lower grinding forces by 2.69–16.44% for the normal force and 4.87–17.44% for the tangential force in comparison to the CG process, owing to the larger undeformed chip thickness of 25.4% for the former one.
2. The UVAG process has a smaller grinding temperature (by 19.01%) and specific grinding energy (by 11.29%) than the other one, resulting in a good cooling fluid convection heat transfer capacity and decreasing the reduction.
3. Multiple cutting edges of abrasive grains are produced because of the alternating load on the top of the grains for UVAG processes, maintaining the sharpness state and eventually reducing the ground surface roughness without remarkable surface defects by 9.87%.

Author contribution Qiang Huang: experimentation, data curation, and writing the original draft. Biao Zhao: data collection and manuscript revision. Yang Cao: experimentation and methodology. Wenfeng Ding: supervision, conceptualization, and methodology. Yucan Fu: resources. Changlan Pu: funding acquisition. Menglan Tang: funding acquisition. Mingming Deng: funding acquisition. Guoliang Liu: funding acquisition.

Funding This work was financially supported by the National Natural Science Foundation of China (Nos. 51921003, 92160301, and 52175415), the Natural Science Foundation of Jiangsu Province (No. BK20210295), and the Foundation of Graduate Innovation Centre in NUAA (No. XCXJH20210503).

Availability of data and material All data generated or analyzed during this study are included in the present article.

Declarations

Ethics approval and consent to participate The article follows the guidelines of the Committee on Publication Ethics (COPE) and involves no studies on human or animal subjects.

Consent for publication Not applicable.

Competing interests The authors declare no competing interests.

References

1. Sales WF, Schoop J, Silva LRR, Machado AR, Jawahir IS (2020) A review of surface integrity in machining of hardened steels. J Manuf Process 58:136–162
2. Wu SX, Liu GD, Zhang WF, Chen WL, Wang CY (2022) Formation mechanism of white layer in the high-speed cutting of hardened steel under cryogenic liquid nitrogen cooling. J Mater Process Technol 302:117469
3. Davis JR (1998) Metals handbook desk edition (second Edition). ASM Int
4. Zhao HY, Huang RR, Sun YM, Tan CW, Wu LJ, Chen B, Song XG, Li GX (2020) Microstructure and mechanical properties of fiber laser welded QP980/press-hardened 22MnB5 steel joint. J Market Res 9:10079–10090
5. Trob N, Brimmers J, Bergs T (2021) Tool wear in dry gear hobbing of 20MnCr5 case-hardening steel, 42CrMo4 tempered steel and EN-GJS-700-2 cast iron. Wear 476:203737
6. Zhou WH, Tang JY, Shao W (2020) Study on surface generation mechanism and roughness distribution in gear profile grinding. Int J Mech Sci 187:105921
7. Sharmin I, Moon M, Talukder S, Alam M, Ahmed MF (2021) Impact of nozzle design on grinding temperature of hardened steel under MQL condition. Mater Today Proc 38:3232–3237
8. Yang ZC, Zhu LD, Zhang GX, Ni CB, Lin B (2020) Review of ultrasonic vibration-assisted machining in advanced materials. Int J Mach Tools Manuf 156:103594
9. Liu B, Tian YB, Han JG, Li LG, Gu ZQ, Hu XT (2021) Development of a new high-shear and low-pressure grinding wheel and its grinding characteristics for Inconel718 alloy. Chin J Aeronaut. https://doi.org/10.1016/j.cja.2021.08.013
10. Tian YB, Li LG, Fan S, Guo QJ, Cheng X (2020) A novel high-shear and low-pressure grinding method using specially developed abrasive tools. Proc Inst Mech Eng Part B J Eng Manuf 235:166–172
11. Ma ZL, Wang QH, Chen H, Chen LY, Qu S, Wang ZX, Yu TB (2022) A grinding force predictive model and experimental validation for the laser-assisted grinding (LAG) process of zirconia ceramic. J Mater Process Technol 302:117492
12. Cao Y, Yin JF, Ding WF, Xu JH (2021) Alumina abrasive wheel wear in ultrasonic vibration-assisted creep-feed grinding of Inconel 718 nickel-based superalloy. J Mater Process Technol 297:117241
13. Cao Y, Zhu YJ, Ding WF, Qiu YT, Wang LF, Xu JH (2021) Vibration coupling effects and machining behavior of ultrasonic vibration plate device for creep-feed grinding of Inconel 718 nickel-based superalloy. Chin J Aeronaut 35:332–345

14. Dai CW, Yin Z, Wang P (2021) Analysis on ground surface in ultrasonic face grinding of silicon carbide (SiC) ceramic with minor vibration amplitude. Ceram Int 47:21959–21968
15. Zhang MH, Pang ZX, Jia YX, Shan CW (2021) Understanding the machining characteristic of plain weave ceramic matrix composite in ultrasonic-assisted grinding. Ceram Int 48:5557–5573
16. Rowe WB, Jin T (2001) Temperatures in high efficiency deep grinding (HEDG). CIRP Ann Manuf Technol 50:205–208
17. Miao Q, Li HN, Ding WF (2020) On the temperature field in the creep feed grinding of turbine blade root: simulation and experiments. Int J Heat Mass Transf 147:118957–118957
18. Rowe WB, Morgan MN, Black SCE (1996) A simplified approach to control of thermal damage in grinding. CIRP Ann Manuf 45:299–302
19. Rowe WB (2017) Temperatures in grinding – a review. J Manuf Sci Eng 139:12
20. Malkin S, Guo C (2007) Thermal analysis of grinding. CIRP Ann Manuf Technol 56:760–782
21. Singh V, Rao PV, Ghosh S (2012) Development of specific grinding energy model. Int J Mach Tools Manuf 60:1–13
22. Jaeger J, Carslaw H (1942) Moving sources of heat and the temperature of sliding contacts. New South Wales 76:202
23. Rowe WB (2001) Thermal analysis of high efficiency deep grinding. Int J Mach Tools Manuf 41:1–19
24. Lavisse B, Lefebure A, Torrance AA (2018) The effects of the flow rate and speed of lubricoolant jets on heat transfer in the contact zone when grinding a nitrided steel. J Manuf Process 35:233–243
25. Chen J, Shi DQ, Miao GL, Yang XG (2017) Effect of maximum temperature on the thermal fatigue behavior of superalloy GH536. Appl Mech Mater 853:28–32
26. Qian N, Ding WF, Zhu YJ (2018) Comparative investigation on grindability of K4125 and Inconel 718 nickel-based superalloys. Int J Adv Manuf Technol 97:1649–1661
27. Yang ZC, Zhu LD, Ni CB, Ning JS (2019) Investigation of surface topography formation mechanism based on abrasive-workpiece contact rate model in tangential ultrasonic vibration-assisted CBN grinding of ZrO2 ceramics. Int J Mech Sci 155:66–82
28. Wu BF, Zhao B, Ding WF (2021) Investigation of the wear characteristics of microcrystal alumina abrasive wheels during the ultrasonic vibration-assisted grinding of PTMCs. Wear 477:203844
29. Chen JB, Fang QH, Wang CC (2016) Theoretical study on brittle–ductile transition behavior in elliptical ultrasonic assisted grinding of hard brittle materials. Precis Eng 46:104–117
30. Pahlitzsch G, Helmerdig H (1943) Determination and significance of chip thickness in grinding. Workshop Technol 12:397–401
31. Zuo DW, Matsuo T (2001) Significance of grinding temperature in metal removal. Key Eng Mater 257:57–60
32. Ramesh K, Huang H, Yin L (2004) Analytical and experimental investigation of coolant velocity in high speed grinding. Int J Mach Tools Manuf 44:1069–1076
33. Winter M, Madanchi N, Herrmann C (2016) Comparative thermal analysis of cutting fluids in pendular surface grinding. Int J Adv Manuf Technol 87:1751–1763
34. Huang WT, Liu WS, Wu DH (2016) Investigations into lubrication in grinding processes using MWCNTs nanofluids with ultrasonic-assisted dispersion. J Clean Prod 137:1553–1559
35. Korpong V, Jirachai M, Teerapat T (2021) Characterization of heat transfer and friction loss of water turbulent flow in a narrow rectangular duct under 25–40 kHz ultrasonic waves. Ultrasonics 114:106366
36. Legay M, Gondrexon N, Person SL (2012) Enhancement of heat transfer by ultrasound: review and recent advances. Int J Chem Eng 43:102221
37. Zhang FL, Huang GW, Liu JM, Du ZJ, Wu SX, Wang CY (2021) Grinding performance and wear of metal bond super-abrasive tools in grinding of Zr-based bulk metallic glass. Int J Refract Metal Hard Mater 97:105501
38. Bhaduri D, Soo SL, Aspinwall DK (2017) Ultrasonic assisted creep feed grinding of gamma titanium aluminide using conventional and superabrasive wheels. CIRP Ann Manuf Technol 66:341–344